Aerodynamic Design of a Morphing Wing Sailplane

Johannes Achleitner[1], Kai Rohde-Brandenburger[2], Paul Rogalla von Bieberstein[2], Fabian Sturm[1] and Mirko Hornung[1]

johannes.achleitner@tum.de

[1]*Institute of Aircraft Design, Technische Universität München, Garching, Germany*

[2]*Institute of Aerodynamics and Flow Technology, German Aerospace Center (DLR) Braunschweig, Germany*

Abstract

The aerodynamic design methodology of a wing with a morphing forward section for an 18 meter class sailplane is shown in this paper. The airfoils have been designed by numerical optimization and reworked using inverse design methods. For the wing planform design a multiple vortex lifting line method has been coupled with an optimization algorithm. Overall aircraft performance calculations indicate the potential of the morphing forward-wing-section concept compared to conventional aircraft.

Nomenclature

c_d	section drag coefficient
c_m	pitching moment coefficient
c_l	section lift coefficient
c_p	pressure coefficient
c	chord
d	airfoil shape design variable
f	objective function
g	inequality constraint function
h	equality constraint function
n	Tollmien Schlichting wave amplification ratio
n_{crit}	critical amplification ratio
p_t	probability density distribution
r	barrier function scaling factor
t	airfoil thickness
$t_{min}(\psi)$	minimum airfoil thickness distribution
$t_{min,tot}$	minimum airfoil thickness
w_i	weight for optimization design point
x	coordinate
x_f	flap end point vector
y	coordinate
C_d	total aircraft drag coefficient
C_{di}	total wing induced drag coefficient
$C_{d,profile}$	total aircraft profile drag coefficient
C_l	total wing lift coefficient
E	lift to drag ratio, glide ratio
N	geometry parameter
Re	Reynolds number
S	wing area
S^*	designated wing area
U_{EAS}	eqivalent air speed
α	angle of attack
δ	flap deflection angle
δ_d	design flap deflection angle
ψ	normalized airfoil coordinate
ζ	normalized airfoil coordinate
Γ	circulation

Subscripts

b	bottom
ell	elliptical
i	index
lim	limit
max	maximum
min	minimum
p	penalized
t	top
tr	transition

Abbreviations

CST	shape function / class function parametrization method
DLM	doublet lattice method
DLR	German Aerospace Center
FEM	finite element method
GPS	Global Positioning System
Idaflieg	Interessensgemeinschaft Deutscher Akademischer Fliegergruppen
RANS	Reynolds averaged Navier Stokes

This article has been reviewed according to the *TS* Fast Track Scheme.
Presented at the AIAA Aviation 2019 Forum, 17-21 June 2019, Dallas, Texas and first published as AIAA-2019-2816

Introduction

Modern racing sailplanes are optimized for the highest possible cross-country speed. Altitude is gained by circling in thermals at low airspeed with accompanied low sink rate. The distance to the next thermal is flown at high speeds, where the speed depends on the expected strength of the thermal. Therefore, the objective of the aerodynamic design is to find the best compromise between climbing performance and high-speed performance. This compromise can be alleviated by changing the shape of the wing. This has been done on sailplanes using camber changing flaps. A new approach is the morphing of the forward section of the wing. Weinzierl et al. [1] showed that a higher maximum lift coefficient of the airfoil in morphed configuration allows a decrease in the wetted area of the wing and an increase in wing loading while keeping the same thermalling and stall speed. This could increase the high-speed performance caused by lower absolute profile drag.

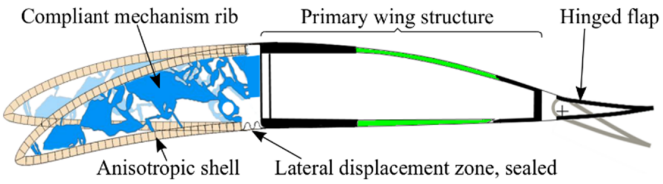

Fig. 1: Structural concept of the morphing wing.

The structural concept is depicted in Fig. 1, showing the undeformed high speed configuration and the morphed low speed configuration combined with a conventional hinged trailing edge flap. Compliant mechanism ribs are intended to precisely deform the forward section of the wing to a high lift airfoil with higher camber. Such ribs are spread over the wingspan approximately every 500 mm. The highly anisotropic wing shell concept is stiff in spanwise direction and compliant to bending deformation in direction of flight [2]. A small compressible section consisting of a corrugated structure as proposed by Yokozeki [3] or a sliding joint connects the morphing section to the primary wing structure. A thin mylar foil acts as an aerodynamic sealing. Boermans [4] proved that this sealing type maintains laminar flow over the flap gap. For roll control and as a second high lift device, a conventional hinged trailing edge flap is used. Similar concepts include those introduced for transport aircraft by the Composite Structures and Adaptive Systems Research Group of the German Aerospace Center (DLR) [5–8] and the FlexSys concept [9, 10]. The main difference of the presented system to the aforementioned concepts is that the leading edge remains on the same developed length both in undeformed and morphing configuration, thus allowing a pure rigid body motion of the leading edge region. The leading edge region can be very sensitive to small contour deviations leading to earlier laminar-turbulent transition or separation. Therefore, this approach enables a system with a more precise deformation behavior, which can be beneficial for the aerodynamic performance of the wing.

Aerodynamic airfoil design for sailplane applications is mostly done by inverse design methods with the 2D panel codes like PROFIL [11] or XFOIL [12], where the pressure distribution is defined by the airfoil designer and the code calculates the airfoil shape from the pressure distribution. These codes have been well validated. The requirement that the rigid part of the airfoil remains unchanged makes inverse airfoil design complex, because the pressure distributions prescribed by the designer for both configurations must ensure this requirement. Also the airfoil leading edge must remain on the same developed length. Numerical shape optimization methods have been used for the aerodynamic design of airfoils for sailplanes [13] and for other applications, i.e. for wind turbine design [14, 15]. Combined with a good parametrization method, geometrical conformity can be ensured for both the undeformed and the morphed configuration. The present work shows the design methodology for airfoils and wing planform and analyzes the potential of this concept for increase in overall aircraft performance. Both the airfoil and the wing planform have been designed using numerical optimization methods.

Airfoil Design and Analysis

Overview

In the present work, the preliminary airfoil design is done by numerical optimization. The optimization methodology for a morphing wing airfoil is shown in Fig. 2 and presented in an overview by Achleitner [16]. A parametrization method calculates the shape of the airfoil from a vector of design variables d_i. The "shape function / class function" parametrization methodology (CST) proposed by Kulfan and Bussoletti [17] has been used for this purpose. Modern laminar airfoils with camber changing flaps have two distinct flap deflection angles, where either the top or the bottom side contour is smooth and kink free, first introduced in the well-known DU89-134/14 airfoil developed by Boermans and van Garrel [4]. In order to parametrize airfoil shapes meeting these characteristics, the CST method has been extended. Another extension of the CST methodology implements a formulation for the representation of the morphing forward section.

The lift and drag properties of the parametrized airfoil in each optimization step are calculated using XFOILSUC [18], a modified variant of the integral boundary layer panel method XFOIL [12] with an improved full e^N transition criterion. In order to improve the prediction of stall onset and post stall behavior a semi empirical shear lag coefficient to shape factor coupling was developed for the XFOIL derivative RFOIL by van Rooij [19]. This coupling equation was implemented in XFOIL 6.99 by Hansen [15] and subsequently implemented in XFOILSUC by the authors. In all XFOIL derivatives, Green's shear lag entrainment equation is implemented, which controls the equilibrium level of the shear stresses in the outer layer of the turbulent boundary layer. The constants $A = 6.7$ and $B = 0.75$ for this G - β locus are used in XFOIL 6.99, based on experimental

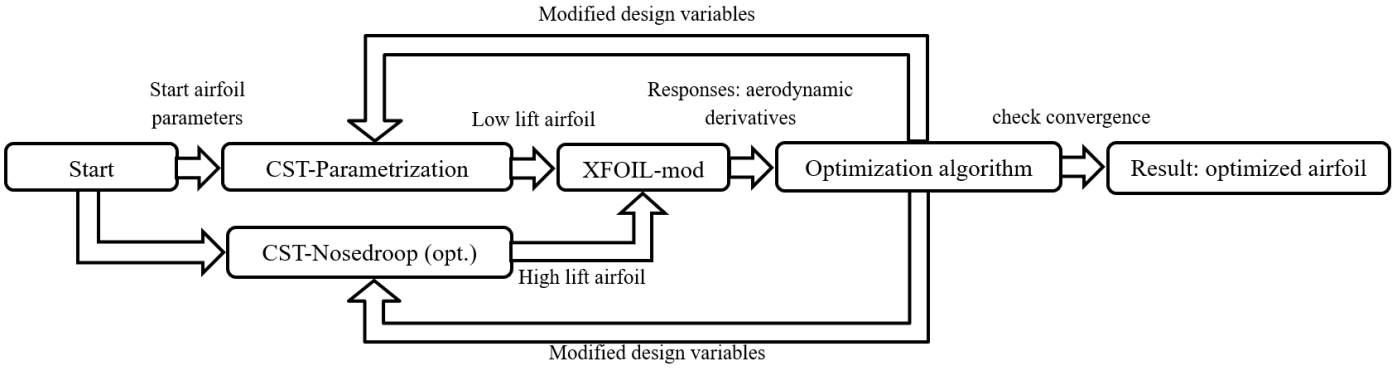

Fig. 2: Airfoil optimization methodology.

data for equilibrium flows. However, van Rooij improved the high lift predictions for wind turbine airfoils by carefully adjusting the coefficients A and B to 6.75 and 0.83, respectively. This adjustment also was used in this paper. XFOILSUC was used for the optimization of the airfoils. However, XFOIL 6.99 with the above mentioned modifications was used for performance analysis for reasons of comparability.

The derivative-free unconstrained optimization algorithm Subplex, originally developed by Rowan [20] is used in this work. The optimized airfoils are reworked using the XFOIL inverse design routine to remove residual waviness of the pressure distribution, to introduce a sharp onset of the adverse pressure gradient after the designated turbulator location and to improve post stall behavior. Subsequently the airfoils stall onset and post stall behavior will be analyzed with the Reynolds number averaged Navier Stokes (RANS) method TAU from DLR, because XFOIL is known to overpredict lift in this region (see [19, 21]).

Airfoil optimization procedure

The numerical optimization problem for the design of the airfoil is given as:

$$\begin{aligned} \min_{\mathbf{d}} \quad & f(\mathbf{d}) = \sum_i w_i \, c_{d,i}(c_{l,i}, \mathbf{d}) \\ s.t.: \quad & g_0(\mathbf{d}) = \max(0, t_{min}(\psi) - t(\psi, \mathbf{d})) \leq 0 \\ & \text{with } \; t(\psi) = \zeta_t - \zeta_b \\ & g_1(\mathbf{d}) = \max(t_{\min,tot} - \max(t(\psi, \mathbf{d})), 0) \leq 0 \\ & g_2(\mathbf{d}) = \zeta_t(\psi, \mathbf{d}) - \zeta_{0.0125,min} \leq 0 \\ & \text{where } \psi = 0.0125\,. \end{aligned} \tag{1}$$

The objective function is a sum of weighted section drag coefficients $c_{d,i}$ at specified section lift coefficients $c_{l,i}$. For both the low-lift undeformed configuration and for the morphed high-lift configuration two drag coefficients at two corresponding lift coefficients $c_{l,i}$ are calculated each. The weights are chosen to correspond to the factor of the ratio of profile drag to overall aircraft drag [4, 22] and the probability density distribution of flight time versus lift coefficient f_t [23, 24]:

$$w_i = \frac{C_{d,profile}(C_{l,i})}{C_d(C_{l,i})} p_t(C_{l,i})\,. \tag{2}$$

The lift coefficient, the weights and the corresponding airfoil configuration for the main wing airfoil are given in Table 1.

Table 1: Optimization specifications for main wing airfoil.

c_l	configuration	$\frac{C_{d,profile}(C_l)}{C_d(C_l)}$	$p_t(C_l)$
0.3	undeformed	0.5	0.33
0.9	undeformed	0.38	0.2
1.3	morphed	0.25	0.2
1.725	morphed	0.25	0.2

The first constraint g_0 in Equation 1 is a constraint for the airfoil thickness, where an arbitrary function $t_{min}(\psi)$ can be specified as minimum thickness. This constraint type is used in this study to ensure a minimum thickness of the flap. The second constraint g_1 is of a similar type, it specifies a minimum total airfoil thickness. Timmer and van Rooij [25] showed a correlation between the top surface coordinate ζ of the airfoil at $\psi = 1.25\%$ and the angle of attack, where leading edge separation occurs. In order to avoid leading edge separation, the constraint g_2 has been introduced, where a minimum ζ coordinate has been introduced. All constraints have been added to the objective functions with a penalty value scheme, because the Sublex optimization algorithm is an unconstrained algorithm and is unable to handle constraints explicitly:

$$f_p = f + \sum_j r_0 \frac{-1}{g_j} + \sum_k r_1 h_k^2\,. \tag{3}$$

The constrained optimization problem is transferred into an unconstrained problem, according to the Sequential Unconstrained Minimization Technique by Fiacco and McCormick [26]. Smooth barrier functions replace the inequality constraints g_j and the equality constraints h_k, which are added

to the original objective function f. For r_0, a small number and for r_1 a large number should be used, so that the barrier functions rise rapidly, when approaching the inequality constraint barrier or leaving the equality constraint center, respectively. It should be mentioned, that no equality constraint is used in the airfoil optimization described in this section, but in the wing planform optimization of section **"Wing Planform Design"**.

Boermans and van Garrel [4] first introduced a flapped laminar airfoil with two distinct flap deflections, the DU89-134/14. The airfoil is designed for the high-performance sailplanes ASW-27, ASH-26 and ASG-29, all produced by Alexander Schleicher Segelflugzeugbau, Germany. At 0° flap deflection, the lower side of the airfoil is smooth and kink free with constant pressure at low lift coefficients up to the turbulator position at 95%c, followed by a sharp, Stratford type turbulent pressure recovery. At 12.5° flap deflection, the upper side is smooth and kink free, thus allowing a long laminar flow region on the upper side without the risk of separation near the flap hinge. This flap deflection angle, is designated here as the design flap angle δ_d. In order to reproduce this characteristics, the CST method has been extended. With the CST method, the top and bottom airfoil contour curves are obtained by multiplying a class function $C(x)$ with a shape function $S(x)$:

$$\begin{aligned} \zeta_b(\psi) &= -C(\psi)\, S(\psi) - N_3\, \psi^2 \quad \text{with} \quad \psi = \frac{x}{c} \quad \text{and} \quad \zeta = \frac{y}{c} \\ \zeta_t(\psi) &= C(\psi)\, S(\psi) + N_3\, \psi^2 + N_4\, \psi^2 . \end{aligned} \tag{4}$$

The trailing edge thickness is represented by the expression $N_3\, x^2$ with $N_3 = t_{TE}/2$. The design flap characteristic is represented by setting an appropriate value for N_3. Therefore the flap end point $\mathbf{x_f} = \binom{\psi_f}{\zeta_f}$ when deflected with the design flap deflection angle δ_d has to be calculated:

$$\begin{aligned} &\mathbf{x_f} = \mathbf{R}_\delta\, (\mathbf{x_{TE}} - \mathbf{x_r}) + \mathbf{x_r} \\ &\text{with} \quad \mathbf{R}_\delta = \begin{pmatrix} \cos(\delta_d) & \sin(\delta_d) \\ -\sin(\delta_d) & \cos(\delta_d) \end{pmatrix} \quad \text{and} \quad \mathbf{x_{TE}} = \binom{1}{0}, \end{aligned} \tag{5}$$

with $\mathbf{x_r} = \binom{\psi_r}{\zeta_r}$ being the flap hinge point. N_4 then results in:

$$N_4 = \frac{\zeta_f}{\psi_f^2} . \tag{6}$$

The class function is defined as:

$$C(\psi) = \psi^{N_1}\, (\psi - 1)^{N_2} \quad \text{with} \quad N_1 = 0.5 \quad \text{and} \quad N_2 = 1 . \tag{7}$$

The first term ensures an infinite slope at the leading edge, whereas the second term ensures a finite trailing edge angle. As shape functions, a weighted sum of Bernstein polynomials are used with the weights being the design variables d_i. Their smooth behavior ensures a smooth airfoil contour:

$$\begin{aligned} S(\psi) = \sum_{i=0}^{n} d_i\, B_i(\psi) \quad &\text{where} \quad B_i(\psi) = K_i\, \psi^i (1-\psi)^{n-i} \\ &\text{and} \quad K_i = \binom{n}{i} = \frac{n!}{i!(n-i)!} . \end{aligned} \tag{8}$$

The airfoil top and bottom contour result from the product of the class function and the sum of the shape functions (Equation 4). A ten parameter CST approximation of the DU89-134/14 airfoil is shown in Fig. 3. The flap top contour has to be de-rotated after CST parametrization to obtain the airfoil contour (red dotted line). The design flap extension allows to parametrize the discontinuous behavior of this feature without requiring extra design variables.

The morphing droop nose also is parametrized with the CST method. First the airfoil contour is decomposed into the camber line and the thickness distribution. Camber line and thickness distribution are then modified by adding a function each. Both functions are given using the CST method with two different class functions. For the camber line change function, the nondimensional ψ coordinate has to be replaced by ψ_c. For the thickness distribution change function, the scaled coordinate ψ_t is used. ψ_s and ψ_e are the coordinates, where the thickness change starts and the morphing section ends:

$$\psi_c = \frac{\psi}{\psi_e} \qquad \psi_t = \frac{\psi - \psi_s}{\psi_e - \psi_s} \tag{9}$$

Because the thickness distribution is not changed in front of the thickness-morphing-starting coordinate ψ_s, the leading edge undergoes only a rigid body motion. For thickness morphing, the class function from Equation 7 is used, but with changed exponents $N_1 = N_2 = 2$. For camber morphing, the following class function can be used:

$$C_c(\psi_c) = (\psi_c - 1)^{N_5} \qquad with \quad N_5 = 3 \tag{10}$$

After changing the camber line and the thickness distribution, the airfoil is reassembled again to obtain the morphed airfoil contour. The ψ coordinates in the morphed region are scaled, so that the leading edge point remains on the same developed length of the top side airfoil contour measured end on from the morphing. The resulting airfoil is shown in Fig. 4 in both undeformed and morphed configuration.

Airfoil optimization results

The optimized airfoil contour and the polar calculated with XFOIL 6.99 (mod) with lift correction of the optimized main wing airfoil is shown in Fig. 5. The airfoil polar of the DU89-134/14 airfoil is shown for reference.

The resulting airfoil *ARS19-124-16-24* is 12.4%c thick, has a camber changing flap of 16%c and a morphing forward section which ends at 25%c. The high section lift coefficient within the laminar low drag bucket[1] of $c_l = 1.75$ can be reached with a nose droop of only 2.4%c. The drag values in undeformed configuration are similar to the DU89-134/14 airfoil at 0° flap deflection, but the laminar low drag bucket is slightly more narrow. The higher section lift coefficient would allow an increase

[1] In some airfoils, called laminar flow airfoils, extensive laminar boundary layer flow and, hence, the minimum drag coefficient extends over a certain range of lift coefficients. This feature is often called "laminar drag bucket".

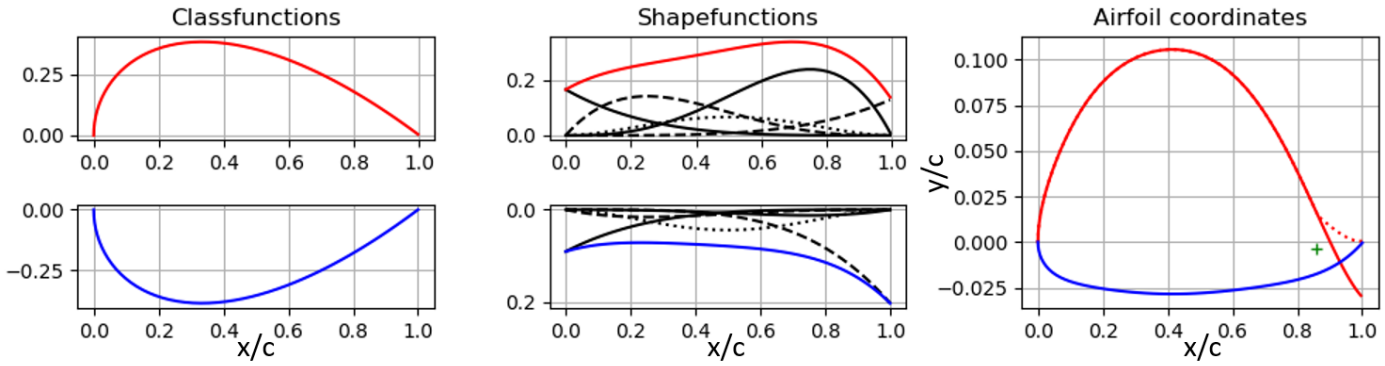

Fig. 3: CST representation of DU89-134/14 airfoil using ten parameters.

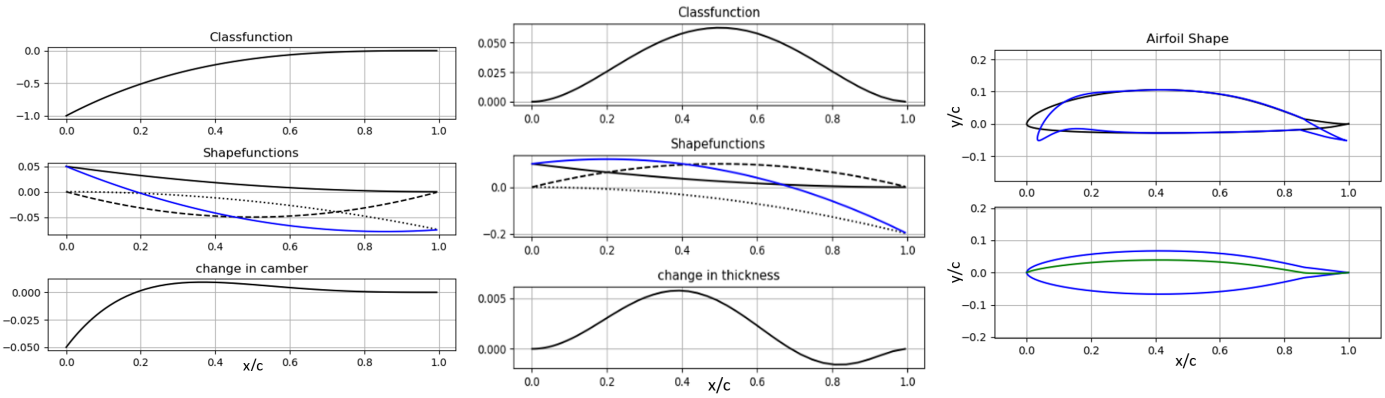

Fig. 4: Classfunctions and shapefunctions for camber line change (left), thickness distribution change (middle) and resulting airfoil shape change (right).

of the maximum wing loading while remaining the same stall speed compared to conventional flapped aircraft. The higher wing loading also results in the same speed range within the laminar low drag bucket in undeformed configuration compared to the DU89-134/14 airfoil at 0° flap setting. However, the lift curve shows a hard decrease in lift beyond the upper corner of the laminar low drag bucket in morphed configuration, which can lead to unfavorable stall behavior. Thus a rework attempt is done trying to improve the stall behaviour in morphed configuration, as explained in the next section.

Airfoil rework

The airfoil rework was done using the inverse design routine of XFOIL. Figure 6 shows the viscous pressure distribution in undeformed and morphed configuration at $\alpha = 1^\circ$ and $\alpha = 5^\circ$, respectively before and after the rework. First the velocity distribution in both configurations have been smoothed. As mentioned in section **"Airfoil Design and Analysis"**, the CST parametrization method is not capable of generating small geometric details. Therefore the pressure distribution on the onset of the main pressure recovery at the turbulator location at 92% x/c on the lower side in undeformed configuration is rounded off on the optimized airfoil instead of having a desired kink. The pressure distribution in the rework has been changed accordingly. Then the leading edge region in morphed configuration has been modified, so that the low pressure spike first occurs at higher angle of attack, thus leading to a gradual forward movement of the transition point and, subsequently, a gradual decrease of lift after $c_{l,max}$. The lift decreases due to a forward movement of the separation point beginning at the trailing edge. As the transition point is moving forward, the boundary layer thickness at the beginning of the pressure recovery section, between 60%c and 70%c, increases. The boundary layer thickness grows faster when the boundary layer is turbulent and not laminar. The thicker the boundary layer, the lower the adverse pressure gradient which can be sustained before separation.

The inverse redesign of a morphing airfoil is an iterative process. Changing the airfoil geometry and therefore the pressure distribution in one configuration leads also to a changed pressure distribution and geometry in the other configuration or a changed morphing distribution. Therefore, the pressure distributions and the required geometry change for morphing have to be carefully modified and analyzed in both configurations over several iteration cycles.

Figure 7 shows the airfoil geometry changes due to the inverse

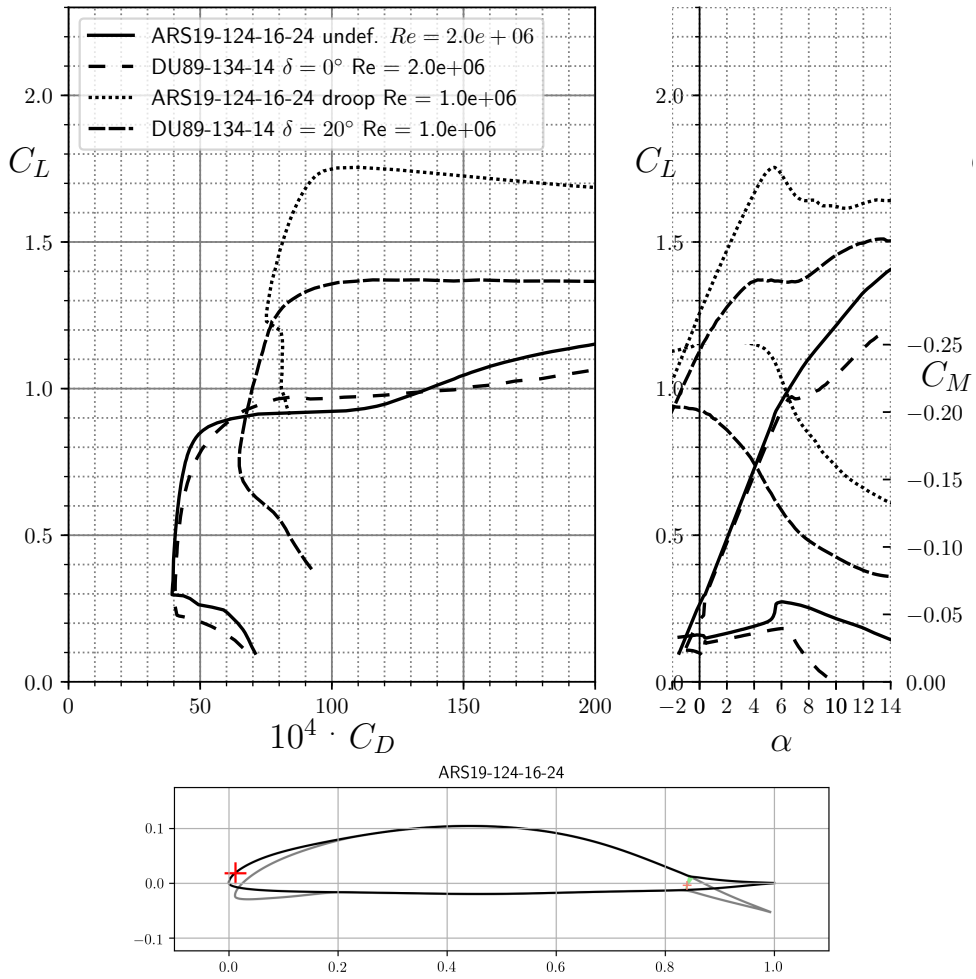

Fig. 5: Polar of the morphing airfoil ARS19-124-16-24 and the DU89-134/14 airfoil calculated with XFOIL 6.99(mod), $n_{crit} = 9$ and ARS19-124-16-24 airfoil shape.

design rework in the forward region. The upper side thickness is increased due to the decreased low pressure spike. On the lower side the pressure distribution is designed to be more continuous, leading to a more continuous curvature in the forward morphing region in front of 25%c and a less abrupt curvature change close to the rigid part of the airfoil. This subsequently leads to an increased width of the laminar low drag bucket in deformed configuration because the short region of constant pressure at 20%c is almost removed, which becomes a region with adverse pressure gradient at lower angles of attack, thus leading to preliminary transition. The disadvantage of this modification is that the drag values increase, as can be seen in the polars in Fig. 8 at lift coefficients between $c_l = 1.3$ and $c_l = 1.7$. These higher drag values are caused by an increase in bubble drag due to the laminar separation bubble in the kink below the flap axis, indicated by the further aft transition location on the lower side compared to the optimized airfoil. But the increased width of the laminar low drag bucket and the more convenient curvature in morphed configuration outweigh this slight performance decrease. A fix could be the use of a dual row pneumatic turbulator system, one at the designated 92%c location on the flap and one in front of the flap hinge line. This though leads to increased complexity of the system.

CFD analysis

XFOIL is known to overpredict lift particularly when turbulent flow separation occurs even when the shape factor to shear lag coefficient coupling is implemented (see Coder and Maughmer [27], Ramanujam and Ozdemir [21]). A RANS - CFD analysis was done to mitigate the risks regarding unfavorable stall characteristics (before conducting an expensive wind tunnel test) instead of relying on an integral boundary layer method only, because similar airfoils have never been designed before. In a preliminary analysis, the DLR-TAU code was used with a one equation Spalart-Allmaras turbulence model [28].

Two different analyses were performed. In the first one, a e^n transition criterion was used. In this analysis, the solution became instationary and did not converge, when the laminar low

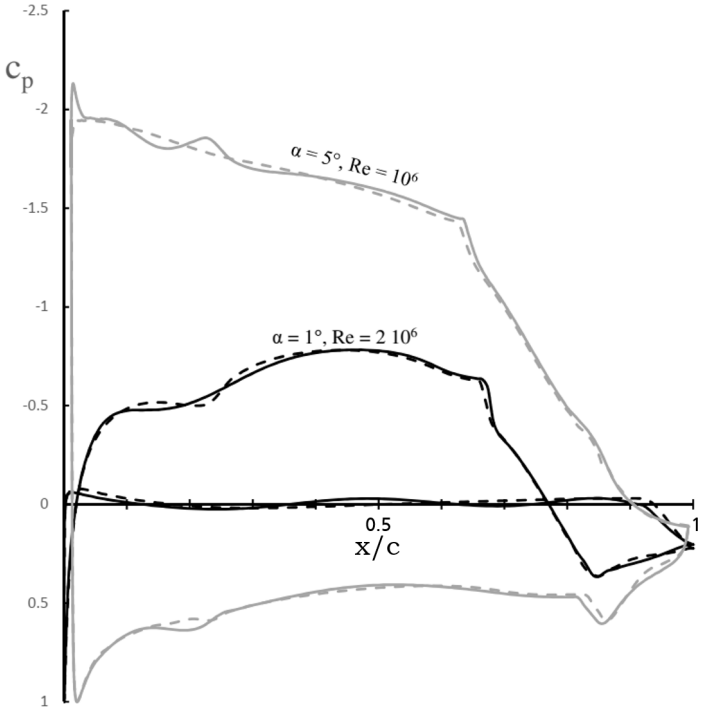

Fig. 6: Viscous pressure distribution of the optimized (solid) and of the reworked (dashed) airfoil in undeformed (black) and morphed configuration (grey).

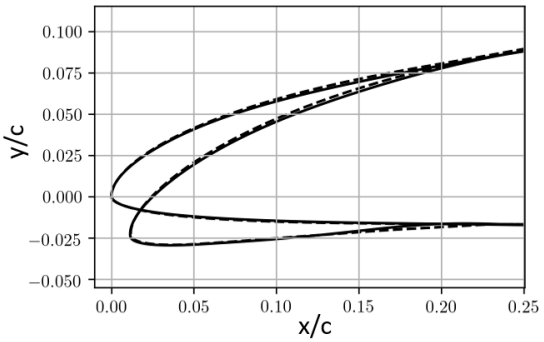

Fig. 7: ASR19-124-16 geometry changes due to airfoil rework. Optimized airfoil (solid lines), reworked airfoil (dashed lines).

drag bucket was exceeded, because the separation location and the transition location interacted. Thus no stationary solution could be found at angles of attack above the laminar low drag bucket. Therefore, a second analysis was performed, in which the transition was fixed to the locations calculated with the modified XFOIL 6.99. The results of the latter and the XFOIL results are shown in Fig. 9. Coder and Maughmer [27] showed that XFOIL normally underpredicts drag within the laminar low drag bucket. Therefore it is not surprising, that the drag values calculated with the DLR-TAU code are higher than those calculated with XFOIL(mod). The lift curve calculated by DLR-TAU with transition locations calculated by XFOIL promises a gentle stall behavior of the new airfoil. Nevertheless, a transient analysis with the DLR-TAU code should be performed to have a better estimate regarding the stall behavior of the new airfoil.

Wing Planform Design

With the methodology shown in section **"Airfoil Design and Analysis"**, five different airfoils have been designed for the wing, shown in Fig. 10. All airfoils have been optimized for the respective Reynolds number range at the location of use on the wing. The two inner airfoils have an increased thickness for structural reasons. The root airfoil is designed for turbulent flow conditions with a main pressure recovery section on the top side with reduced gradient. This also leads to a forward movement of the location of maximum thickness, which is beneficial for the main spar structural design in combination with an increased chord length at the root. The two outer wing airfoils are designed to have a lift reserve at angles of attack at and beyond $c_{l,max}$ compared to the inner wing airfoils for a gentle overall aircraft stall behavior. Also the flap depth was increased by 1% to compensate loss of lift in morphed configuration due to viscous effects caused by the lower Reynolds numbers at the outermost airfoil. The PS-01 airfoil has been used for the winglet, also shown in Fig. 10.

A second optimization formulation was created for wing planform design. Before the optimization, the airfoils were twisted to operate at the same zero lift angle of attack. The optimization problem is given in equation 11. The design variables are the chord lengths c_i at eight spanwise stations, thus resulting in a multi-tapered wing with seven trapezoidal sections. As an objective function used was the relation between the induced drag coefficient C_{di} and the induced drag coefficient with elliptical circulation distribution $C_{di,ell}$. Two wing lift coefficients have been analyzed. In the morphed configuration, a lift coefficient of $C_l = 1.6$ was set, whereas in the undeformed configuration a lift coefficient of $C_l = 0.4$ was set. An equality constraint was implemented to restrain the wing area to the wing area constraint value $S^* = 8.6\,\mathrm{m}^2$. A second constraint limited the lift coefficient to a distribution defined by a polygonal line for a gentle stall behavior. The resulting circulation distribution of the wing was obtained by the multi-lifting-line method Lifting_Line developed by Horstmann [29]. The Subplex optimization algorithm already used for the airfoil optimization was also used for the planform optimization. The constraints again were handled by adding penalties to the objective function. Both constraints were added according to Equation 3.

$$\begin{aligned} \min_{\mathbf{c}} &: f(\mathbf{c}) = \sum_i \frac{C_{di,i}}{C_{di,ell,i}} \\ s.t. &: g_0(\mathbf{c}) = \max\left(\frac{c_l(y)}{c_{l,lim}(y)}\right) - 1 \leq 0 \\ &: h_1(\mathbf{c}) = \frac{S}{S^*} - 1 = 0 \end{aligned} \tag{11}$$

The initial design variables were set so that the planform

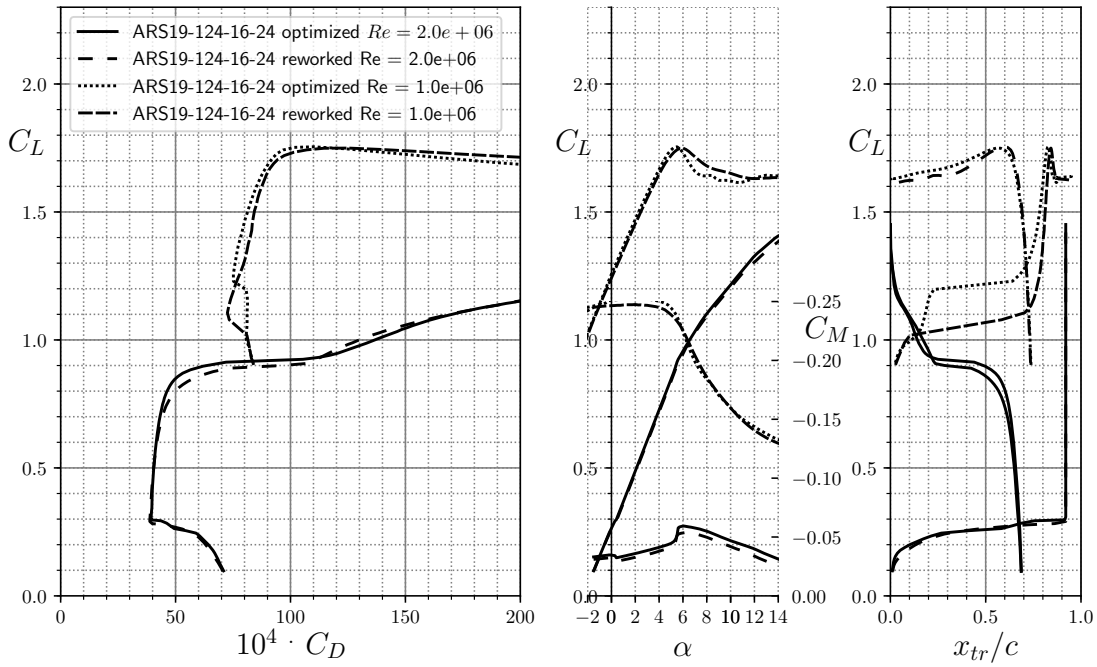

Fig. 8: Comparison of optimized and reworked airfoil polars. Drag polar (left), lift curve (middle) and transition location (right) calculated with XFOIL 6.99 (mod), $n_{crit} = 9$.

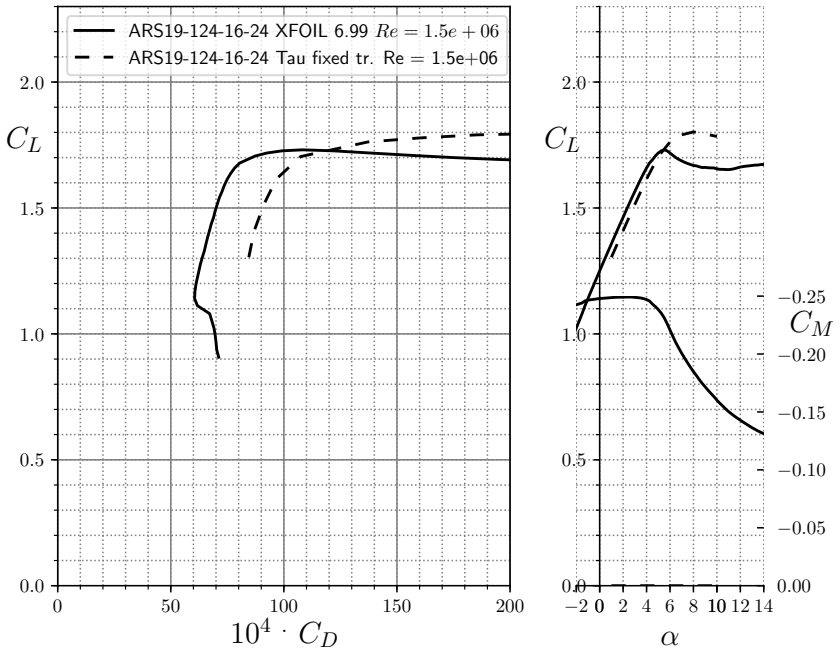

Fig. 9: Comparison of polars in morphed configuration calculated with XFOIL 6.99 (mod), $n_{crit} = 9$ and with DLR-TAU.

touches an ellipse with with a major axis being the developed wing span and the minor axis being set, so that $S = S^*$. This start design was chosen, because an elliptical planform almost gives an optimal elliptical lift distribution, if the airfoils are similar and the twist is small. The winglet was designed manually on the initial design. The objective was that the lift distribution be as close to being elliptic in both configurations, with emphasis on the undeformed configuration so that the winglet creates no additional drag at high speeds. An ample lift reserve at the high lift coefficient was implemented for the case of yaw move-

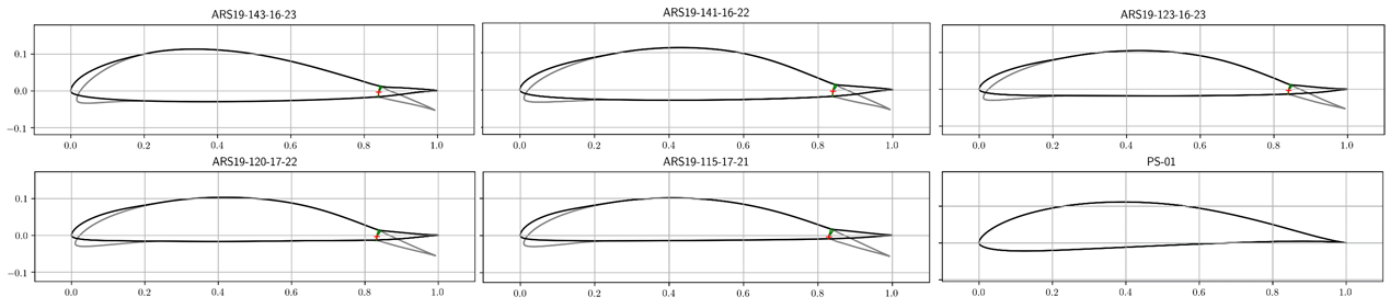

Fig. 10: Airfoils of the morphing wing, root airfoil (top left) to winglet airfoil (bottom right).

ment during thermalling. The lift coefficients should lie within the laminar low drag bucket of the winglet airfoil at both design lift coefficients. The winglet should further be optimized using numerical optimization methods with CFD analysis with a RANS method in a future study. The dihedral of the wing was 3.25°. For the optimization, the dihedral distribution was chosen, so that the front view corresponds to the wing deformation in static straight flight condition with an airspeed of 95 kph. The deformations were taken from a preliminary design coupled FEM/DLM analysis performed in NASTRAN.

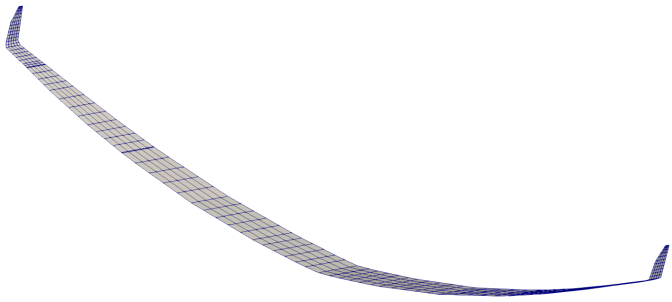

Fig. 11: 3D view of the optimized wing including the panel distribution.

A 3D view of the optimized wing and the panel distribution is shown in Fig. 11. The circulation distribution and the optimal elliptical lift distribution according to Munk's third theorem [30] are shown in Fig. 12. It can be seen that the circulation distribution is close to the optimal elliptical distribution at both lift coefficients. The winglet operates well within the laminar low drag bucket of the winglet airfoil between $c_l = 0.55$ and $c_l = 1.25$. A low induced drag coefficient of 96 % compared to the elliptical circulation distribution of a planar wing was achieved in both configurations.

Aircraft Performance Estimation

For the assessment of the aircraft polars, the Lifting_Line wing model from section **"Wing Planform Design"** with the optimized planform was used. The horizontal and vertical tail of the 18 meter class, high performance sailplane ASG-29 were added to the model. A trim calculation was done for every lift coefficient in order to calculate the elevator deflection angles. Subsequently, the induced drag was calculated. Then the profile drag of both wing and tailplane was calculated by interpolation of the airfoil polars in lookup tables for all airfoils generated by the modified XFOIL version. For comparison, a second model was created of the ASG-29 wing and tailplane using the same method.

For the calculation of the fuselage and residual drag, data was used from a performance measurement of the ASG-29 aircraft. The measurement was done by the *Idaflieg* and DLR on August 17, 2008, using the well known differential measurement method by Wende [31] and the improvements by Paetzold [32]: sink rate differences between a calibrated reference aircraft and the specimen aircraft are measured using differential-GPS. The induced drag and the profile drag of the ASG-29 then were calculated using the above mentioned Lifting_Line model and the lookup table method for three different flap deflection angles (0°, 10° and 20°) with the same take off mass and position of center of gravity as in the measurements. The sum of fuselage drag and residual drag due to interference effects then was calculated by subtracting the calculated profile drag and induced drag from the total drag obtained from the measurement data. Hence, three residual drag polars were calculated for each flap setting. Furthermore an envelope polar for the fuselage and residual drag as a function of the angle of attack was generated using the three single polars for the respective flap deflections.

The overall aircraft polars of the morphing wing sailplane and the ASG-29, both at maximum takeoff mass of 600 kg in Fig. 13 then were obtained by adding the envelope residual drag to the induced drag calculated with Lifting_Line and the profile drag calculated using the lookup tables.

In Fig. 13, the calculated glide ratio versus airspeed is shown for the morphing wing aircraft and the ASG-29 aircraft (blue lines), both at maximum mass of 600 kg. This corresponds to a wing loading of 57 $\mathrm{kg/m^2}$ for the ASG-29 and 69 $\mathrm{kg/m^2}$ for the morphing wing aircraft. The calculation indicates that a wing loading up to 69 $\mathrm{kg/m^2}$ can be reached with the morphing wing concept by maintaining a minimum speed of 90 km/h as required by the certification specification CS22 [33]. This enables better glide ratios at speeds above 140 km/h compared to the ASG-

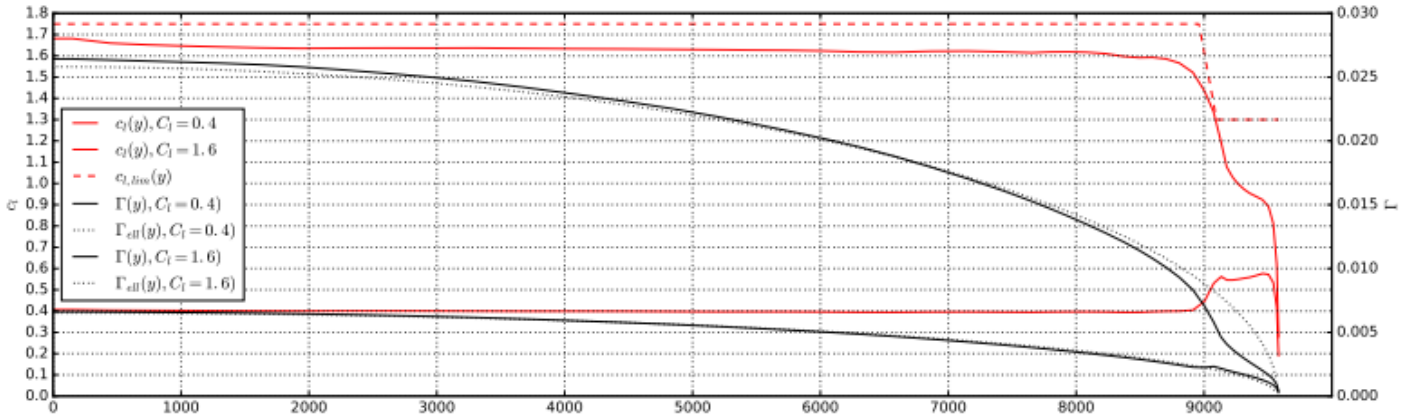

Fig. 12: Circulation distribution, elliptical circulation distribution, lift coefficients and lift coefficient limit of the undeformed configuration at $C_l = 0.4$ and the morphed configuration at $C_l = 1.6$.

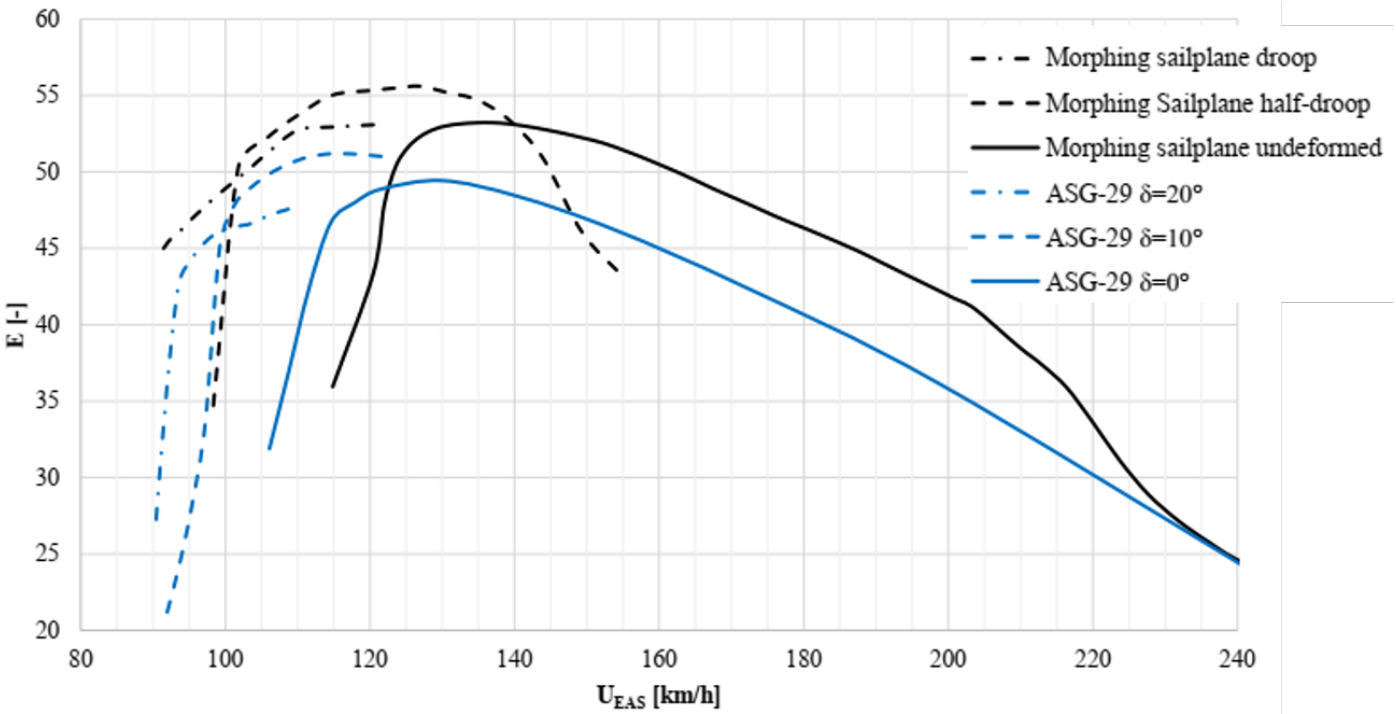

Fig. 13: Calculated glide ratio vs. airspeed of the ASG-29 and the morphing wing sailplane, both at 600 kg take off mass.

29, while having a slightly better low speed thermalling performance due to lower sink rates in the low-speed range. According to the analysis, about 20 km/h higher inter-thermal flight speeds can be expected with the same glide ratio. Also the best glide ratio is expected to be increased by approximately 8.5% due to the reduced overall profile drag. However, as the interference drag is considered to be equal to the ASG-29 in this study, special attention has to be paid on the design of the wing root junction and the winglet root.

A second prerequisite to reach the calculated performance improvement is the achievement of precise deformation of the airfoil contour and low waviness along the whole wing span. And, the sealing of the slit between the morphing section and the rigid wing has to be carefully designed and manufactured, so that the laminar flow passes the gap without transition. Although the airfoil pitching moment coefficients of the morphing wing airfoil as shown in Fig. 8 are higher than the pitching moments of the DU89-134/14 airfoil, the absolute pitching moment is lower due to the fact that it scales with the chord length squared, which is about 20% lower on the morphing wing sailplane. Therefore the horizontal tailplane could be reduced in area, which would result in a slight performance gain.

Conclusions

This paper describes the design methodology of a morphing wing aircraft has been shown. A morphing airfoil was designed using numerical optimization methods. The optimization results demonstrate a remarkable increase of lift compared to conventional flapped airfoils. The resulting airfoil also showed low drag values but suffered from detrimental stall characteristics. Therefore rework was done using inverse design methods. According to XFOIL calculations, a gentle stall behavior could be achieved without a significant performance loss. To check this stall behavior, a CFD analysis with the DLR TAU code was performed and confirmed the gentle stall behavior and similar $c_{l,max}$. A wind tunnel test campaign is planned to prove the calculated performance improvement.

The wing planform design was done using a numerical optimization environment using the multi lifting line method Lifting_Line for the calculation of the lift distribution and induced drag. The winglet was designed with a conventional method and will be optimized in a future study using numerical optimization and CFD analyses. The aircraft overall performance calculation was done using the same multi lifting line method as for the planform design for calculating the induced drag. The tail was taken from the ASG-29 plane and added to the model. Profile drag was calculated with a lookup-table method from polars calculated with XFOIL 6.99 (mod) and the fuselage drag was estimated with an analytical relation.

The overall aircraft performance of the morphing wing aircraft was compared with the ASG-29 production sailplane, manufactured by Alexander Schleicher Segelflugzeugbau, Germany. The calculations indicate a significant performance increase of about 8.5% better maximum glide ratio and 20 km/h inter thermal flight speeds at the same glide ratio. However, this requires a precise deformation of the airfoils and junctions between wing and fuselage and wing and winglet designed with low additional drag. Therefore a CFD analysis and design optimization should give more insight.

Acknowledgements

The present studies have been funded under the grant of the German Federal Aviation research program LuFo V-3 (Luftfahrtforschungsprogramm V-3). The authors would like to acknowledge the support of the German Federal Ministry for Economic Affairs and Energy.

References

[1] Weinzierl, M., Achleitner, J., and Baier, H., "Highly Extensible Skin of a Variable Geometry Wing Leading Edge of a High-Performance Sailplane." *Technical Soaring*, Vol. 39, No. 1, 2015, pp. 4–9.

[2] Achleitner, J. and Baier, H., "CellSkin-a new flexible shell structure for a morphing wing aircraft." *Konferenzbeitrag, ICCS19 - Proceedings of the 19th International Conference on Composite Structures*, 2016, pp. 143.

[3] Yokozeki, T., Takeda, S.-i., Ogasawara, T., and Ishikawa, T., "Mechanical properties of corrugated composites for candidate materials of flexible wing structures." *Composites Part A: Applied Science and Manufacturing*, Vol. 37, No. 10, 2006, pp. 1578–1586.

[4] Boermans, L. and van Garrel, A., "Design and Windtunnel Test Results of a Flapped Laminar Flow Airfoil for High-Performance Sailplane Applications." *ICAS 19 - Proceedings of the 19th Conference of the International Council of Aeronautical Sciences*, 1994, pp. 1241–1247.

[5] Kintscher, M., Peter Monner, H., Kühn, T., Wild, J., and Wiedemann, M., "Low speed wind tunnel test of a morphing leading edge." *AIDAA - Italian Association of Aeronautics and Astronautics XXII Conference*, 2013.

[6] Radestock, M., Riemenschneider, J., Monner, H.-P., and Rose Michael, "Structural optimization of an UAV leading edge with topology optimization." *DeMEASS Design, Modelling and Experiments of Advanced Structures and Systems Conference*, 2014.

[7] Sinapius, M., Monner, H. P., Kintscher, M., and Riemenschneider, J., "DLR's Morphing Wing Activities within the European Network." *23rd International Congress of Theoretical and Applied Mechanics, ICTAM2012*, 2014, pp. 416–426.

[8] Vasista, S., de Gaspari, A., van de Kamp, B., Riemenschneider, J., Monner, H. P., and Ricci, S., "Compliant structures-based wing and wingtip morphing devices." *Aircraft Engineering and Aerospace Technology*, Vol. 88, No. 2, 2016, pp. 311–330.

[9] Kota, S., A. Hetrick, J., Osborn, R., Paul, D., Pendleton, E., Flick, P., and Tilmann, C., "Design and application of compliant mechanisms for morphing aircraft structures." *Proc SPIE*, Vol. 5054, 2003.

[10] Lu, K.-J., *Synthesis of Shape Morphing Compliant Mechanisms*, Dissertation, University of Michigan, 2004.

[11] Eppler, R. and Somers, D. M., "Low Speed Airfoil Design and Analysis. Advanced Technology Airfoil Research." *Advanced Technology Airfoil Research - Volume I, NASA CP-2045, Part 1*, 1979, pp. 73–99.

[12] Drela, M., "XFOIL: An Analysis and Design System for Low Reynolds Number Airfoils." *Low Reynolds Number Aerodynamics Conf. Proc.*, 1989.

[13] Kubrynski, K., "Design of a Flapped Laminar Airfoil for High Performance Sailplane." *30th AIAA Applied Aerodynamics Conference*, 2012, pp. 94–115.

[14] Grasso, F., "Design of a family of new advanced airfoils for low wind class turbines." *Journal of Physics: Conference Series*, Vol. 555, 2014, pp. 012044.

[15] Hansen, T. H., "Airfoil optimization for wind turbine application." *Wind Energy*, Vol. 21, No. 7, 2018, pp. 502–514.

[16] Achleitner, J., Rohde-Brandenburger, K., and Hornung, M., "Airfoil optimization with CST-parameterization for (un-)conventional demands." *XXXIV OSTIV Congress Program and Proceedings*, 2018, pp. 117–120.

[17] Kulfan, B. and Bussoletti, J., "Fundamental Parameteric Geometry Representations for Aircraft Component Shapes." *11th AIAA/ISSMO Multidisciplinary Analysis and Optimization Conference*, Multidisciplinary Analysis Optimization Conferences, American Institute of Aeronautics and Astronautics, 2006.

[18] Bongers, J., *Implementation of a new transition prediction method in xfoil*, Masters thesis, TU Delft, Delft, Netherlands, 2008.

[19] van Rooij, R., *Modification of the boundary layer calculation in RFOIL for improved airfoil stall prediction*, Tech report iw-96087r, TU Delft, 1996.

[20] Rowan, T. H., *Functional Stability Analysis of Numerical Algorithms*, Dissertation, University of Texas, Austin, 1990.

[21] Ramanujam, G. and Ozdemir, H., "Improving Airfoil Lift Prediction." *35th Wind Energy Symposium 2017*, Curran Associates Inc, Red Hook, NY, 2017, p. 1.

[22] Thomas, F., *Grundlagen für den Entwurf von Segelflugzeugen*, Motorbuch Verlag, Stuttgart, 2nd ed., 1984.

[23] Scherrer, M., "Flight Template: A tool for optimizing aerodynamics at the design stage." *Technical Soaring*, Vol. 32, No. 3, 2008, pp. 85–92.

[24] Maughmer, M. D., Coder, J. G., Wannenmacher, C., and Würz, W., "The Design of a New Racing Sailplane: A New Thermal Mix Model and the Role of Transitional CFD." *17th AIAA Aviation Technology, Integration, and Operations Conference*, American Institute of Aeronautics and Astronautics, Reston, Virginia, 2017, p. 87.

[25] Timmer, W. A. and van Rooij, R. P. J. O. M., "Summary of the Delft University Wind Turbine Dedicated Airfoils." *Journal of Solar Energy Engineering*, Vol. 125, No. 4, 2003, pp. 488.

[26] v. Fiacco, A. and McCormick, G. P., "The Sequential Unconstrained Minimization Technique for Nonlinear Programing, a Primal-Dual Method." *Management Science*, Vol. 10, No. 2, 1964, pp. 360–366.

[27] Coder, J. G. and Maughmer, M. D., "Comparisons of Theoretical Methods for Predicting Airfoil Aerodynamic Characteristics." *Journal of Aircraft*, Vol. 51, No. 1, 2014, pp. 183–191.

[28] Spalart, P. and Allmaras, S., "A One-Equation Turbulence Model for Aerodynamic Flows," *30th AIAA Aerospace Sciences Meeting and Exhibit*, American Institute of Aeronautics and Astronautics, 1992.

[29] Horstmann, K.-H., "Ein Mehrfach-Traglinienverfahren und seine Verwendung für Entwurf und Nachrechnung nichtplanarer Flügelanordnungen." *DFVLR-FB–87-51*, 1987.

[30] Munk, M. M., "The Minimum Induced Drag of Aerofoils." *NACA-TR-121*, 1923.

[31] Wende, G., *Ermittlung der Flugleistung von Segelflugzeugen*, Dissertation, TU Braunschweig, 2003.

[32] Pätzold, F., *Windmessung mittels Segelflugzeug*, Dissertation, Technische Universität Braunschweig, 2018.

[33] European Union Aviation Safety Agency, *Certification Specifications for Sailplanes and Powered Sailplanes CS-22: Amendmend 2*, 5 March 2009.